Significance of ionic wind propulsion on charged particle removal during flue gas purification

Yifan Wang [a], Wenchao Gao [b], Hao Zhang [a], Zhengda Yang [c], Zhongyang Zhao [a], Lingyu Shao [a], Zunqiang Sun [a,d], Chenghang Zheng [a,*], Xiang Gao [a,*]

[a] State Key Lab of Clean Energy Utilization, State Environmental Protection Engineering Center for Coal-Fired Air Pollution Control, Zhejiang University, 38 Zheda Road, Hangzhou 310027, People's Republic of China
[b] Beijing Institute of Nanoenergy and Nanosystems, Chinese Academy of Sciences, Beijing 100083, People's Republic of China
[c] College New Energy, China University of Petroleum East China, Qingdao 266580, People's Republic of China
[d] State Power Environmental Protection Research Institute Co., Ltd, Nanjing 210031, People's Republic of China

HIGHLIGHTS

- A comprehensive particle removal model considered ionic wind is developed.
- The flow field is visualized through different presentations to indicate ionic wind performance.
- The roles of ionic wind in particle transport and deposition are quantified.
- A novel electrostatic precipitator is proposed to improve removal performance.

GRAPHICAL ABSTRACT
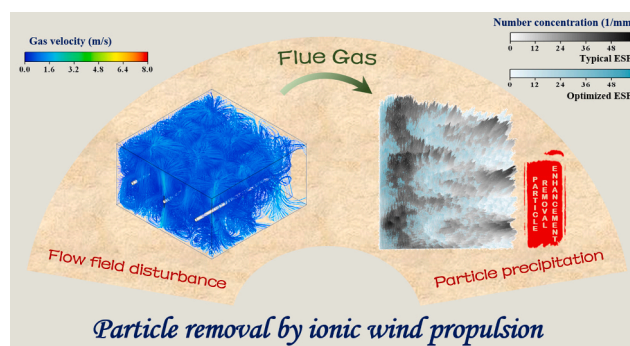
ARTICLE INFO

ABSTRACT

Ionic wind propulsion plays a vital role in charged particle transport during flue gas purification, which is closely related to high-efficiency particulate removal. Here, we establish a comprehensive model to investigate the effect of ionic wind on the transport and deposition of charged particles. The high-speed ionic wind disturbs the space flow field in a meaningful way, which also causes the formation of 'U'-shaped high-speed zones within the near-plate region. After the dusty flue gas enters the electrostatic field, due to the disturbance of high-speed ionic wind, apart from the electric force, particle transportation is acted by ionic wind propulsion. Charged particles can be significantly accelerated with ionic wind propulsion, while it also introduces an uneven distribution of deposited particles. Based on these findings, a novel electrostatic precipitator is proposed to optimize the space flow field, and the collection efficiency and dust layer shape are both significantly improved.

1. Introduction

The various resulting problems due to environmental pollution have become a global concern [1]. Among them, particulate matter (PM) pollution has a detrimental effect on the environment, which is closely related to people's lives and has become an essential obstacle to global development [2]. Decades of research have shown that ambient pollution by PM, especially fine particulate matter (PM$_{2.5}$), increases the amount and seriousness of lung and heart disease and other health problems [3]. Meanwhile, PM is the main cause of reduced visibility (haze) around the world [4]. Although this atmospheric environment may be affected by natural factors, anthropogenic activities account for the vast majority of negatively influencing factors, such as industrial emissions, automobile exhaust, and garbage incineration [5].

How to minimize PM emission at the source has been one of the paramount topics. Various methods have been deployed to control pollutant emissions over the past years, with electrostatic precipitation as one of the highly promising and widespread technologies in flue gas purification [6]. This method has been extensively applied to remove particulate and heavy metals from flue gas in many industries, such as coal-fired power plants, biomass power plants, and metallurgical plants [7,8]. It is also used for the removal of multiple pollutants in indoor air [9,10]. Moreover, this method is considered to be one of the potential dust mitigation technologies for future lunar exploration [11]. However, challenges still exist in practical applications, especially when the inlet PM concentration is high or particle resistivity is low, which may introduce the occurrence of dust re-entrainment and hinder ultralow PM emission [12]. The core and focus of solving this problem is how to optimize the flow field and take into account its impacts between particle transport and dust layer stability. Significantly, the vital role of ionic wind (also called electric wind or electrohydrodynamic (EHD) flow) in this process cannot be ignored, which can further contribute to the complexity of the flow field [13].

Understanding charged particle migration and deposition with ionic wind propulsion is closely linked to enhancing fine particle removal in the electric field [14,15]. Ionic wind is created by the EHD propulsive force in electrically charged fluids, which includes the exchange of mass, momentum, and energy [16]. In principle, ionization near the discharge electrode produces electrons that drift toward the grounded plates, which are accelerated by the electric field and collide with neutral air molecules. These high-frequency collisions and the momentum exchange produce a body force that leads to the generation of ionic wind, which consists of ionized and neutral air molecules (see Fig. S1a) [17,18]. In addition to particle removal, ionic wind has also been extensively applied in many fields, as shown in Figs. S1b-S1j.

Recently, many efforts have been made toward discovering the flow field disturbance associated with ionic wind in terms of power supply [19,20], electrode configuration [21,22], flue gas composition [23,24], etc. Among them, particle image velocimetry (PIV) is a typical method to investigate the particle flow field, which indicates that particle migration is significantly affected by the disturbance induced by the ionic wind [25]. The charged particles reciprocate in the electrostatic field because of the formation of local reverse flow instead of direct transport to the grounded plates [26,27]. However, this method also has limitations. For example, it is difficult to observe the microscopic flow field near the needle tips and to match the flow field in situ with the electric field.

Computational fluid dynamics can be considered a complementary method to obtain some other data, which are difficult to measure by experimental methods [28]. An understanding of how the electric field and flow field detailed distributions contributed to further evaluation of particle migration performance under the disturbance of ionic wind. Previously, various dedicated efforts and models have been carried out to investigate the role of ionic wind in the space flow field and particle collection with different flue gas components [29,30] and electrode configurations [14,31]. However, these studies mainly focus on wire electrodes rather than spike electrodes, which demonstrate stronger corona-discharge characteristics and can generate stronger ionic wind. Recently, some researchers have tried to evaluate particle removal performance with complicated electrodes by numerical methods [22,32]. On this basis, high gas velocity and strong flow-field disturbance were visualized to change people's perception of ionic wind in the electrostatic field [33]. Nevertheless, these works are limited to the comparison between the applied voltage and total particle collection efficiency. In fact, particle transport performance and detailed deposition distribution are also important parameters in practical applications, which can also be influenced by ionic wind [34]. Thus, having fundamental knowledge about particle migration and deposition performance under ionic wind propulsion is crucial in the promotion of electrostatic precipitator (ESP) development with increasingly stringent PM emission levels [13].

Herein, the roles of ionic wind in flow field disturbance and charged particle removal are thoroughly investigated by a comprehensive model. The flow field is visualized through different presentations to evaluate ionic wind performance within the space. Meanwhile, due to the disturbance of high-speed ionic wind, apart from the electric force, particle transportation also be acted by ionic wind propulsion, which will eventually reflect the uneven distribution of deposited particles. Based on these findings, a novel ESP is proposed to optimize the space flow field and particle removal performance. This research is of considerable significance in the development of multiphase flow models and the innovation of PM emission control technology.

2. Methods

The physical model of ionic wind generation and particle deposition in the electric field is established by the theoretical analysis of multi-process coupling (corona discharge, gas flow, particle charging, and particle transport). These sub-processes are described by the relevant governing equations and interact with each other. Herein, the comprehensive model is applied to investigate the vital role of ionic wind propulsion in the space flow field and charged particle migration. In addition, this model can serve as a reference for investigations of charged micro- to nano-scale particles, such as electrodeposition, electrostatic manipulation, and nano 3D printing.

2.1. Corona discharge

The foundations of electric field and ionic wind generation are laid by corona discharge. In this study, the distributions of the electric field and ion density field are described by Poisson's equation and the current continuity equation, respectively.

Poisson's equation is described by the formula:

$$\nabla^2 \varphi = -\rho_{ion}/\varepsilon_0 \tag{1}$$

The current continuity equation is as follows:

$$\nabla \cdot \vec{J} = \nabla \cdot \left[\rho_{ion} \left(k_{ion} \vec{E} + \vec{u} \right) - D_{ion} \nabla \rho_{ion} \right] = 0 \tag{2}$$

$$\vec{E} = -\nabla \varphi \tag{3}$$

where φ represents the electric potential, ρ_{ion} represents the space ion density, ε_0 represents the gas permittivity, J represents the current density, k_{ion} represents the ion mobility, E represents the electric field strength, u represents the gas velocity, and D_{ion} represents the ion diffusion coefficient.

The electric field strength on the discharge electrode surface (E_S) can be calculated by Peek's law:

$$E_S = E_0 m \left(\delta + 0.0308 \sqrt{\frac{\delta}{r_0}} \right) \tag{4}$$

where E_0 represents the constant of the breakdown electric field strength, and 3.1×10^6 V/m was used in this simulation. m represents the dimensionless surface parameter, and 0.25 was used in this simulation. δ represents the relative gas density, and r_0 represents the curvature radius of the discharge electrode.

2.2. Gas flow

The mixture airflow passing through the electric field can be assumed to be a steady-state and incompressible turbulent flow and is described by the RNG k-epsilon model. The governing equations are described below.

The conservation of momentum is defined as:

$$\rho_{gas}\left(\frac{\partial \vec{u}}{\partial t} + \vec{u}\cdot\nabla\vec{u}\right) = -\nabla P + (\mu + \mu_t)\nabla^2\vec{u} + \rho_{ion}\vec{E} \tag{5}$$

The conservation of mass is defined as:

$$\nabla\cdot(\rho_{gas}\vec{u}) = 0 \tag{6}$$

where ρ_{gas} represents the gas mass density, P represents the absolute pressure, μ represents the dynamic viscosity, and μ_t represents the turbulent eddy viscosity.

2.3. Particle charging

When the free ions are captured by particles in the electric field, the phenomenon is called particle charging. The charging process can be expressed by the two mechanisms of field charging and diffusion charging. Field charging requires the presence of an electrical field to drive the free movable charge carriers, whereas diffusion is based on the random movement of gas ions caused by temperature and described by the kinetic gas theory. Many attempts have been made by scholars worldwide to reasonably combine these two mechanisms. After comparing various charging models [35,36], the one proposed by Lawless [37] is adopted, as it offers a better compromise between accuracy and simplicity. The dimensionless form of this model is presented as follows:

$$\frac{dq_p}{dt} = \begin{cases} \dfrac{q_s}{\tau}\left(1 - \dfrac{q}{q_s}\right)^2 + \dfrac{2\pi\alpha\rho_{ion}k_{ion}k_Bd_p}{e} & q \le q_s \\[4mm] \dfrac{\alpha}{4\tau}\dfrac{(q-q_s)}{exp\left(\dfrac{e(q-q_s)}{2\pi\varepsilon_0 k_{ion}k_BTd_p}\right)-1} & q > q_s \end{cases} \tag{7}$$

$$\alpha = \begin{cases} 1 & e_{norm} < 0.525 \\[3mm] \dfrac{1}{(e_{norm}+0.457)^{0.575}} & e_{norm} > 0.525 \end{cases} \tag{8}$$

$$e_{norm} = \frac{ed_p}{2k_BT}E \tag{9}$$

$$q_s = 3\frac{\varepsilon_r}{\varepsilon_r+2}\pi\varepsilon_0 d_p{}^2 E \tag{10}$$

$$\tau = \frac{4\varepsilon_0}{\rho_{ion}k_{ion}} \tag{11}$$

where q_p represents the particle charge, q_s represents the particle saturation charge, k_B represents the Boltzmann constant, d_p represents the particle diameter, τ represents the time constant, e represents the unit charge, T represents the gas temperature, and ε_r represents the particle relative permittivity.

2.4. Particle transport

In a gas–solid two-phase flow, the forces acting on a particle include drag, electric, Brownian, Saffman lift, buoyancy, virtual mass, thermophoresis, and pressure gradient forces [38]. Among them, the Saffman lift, buoyancy, and virtual mass can be ignored since they are orders of magnitude smaller than the inertial force. Thermophoresis is related to the temperature difference, which is small in this electric field. The pressure gradient force is only considered when the particle density is small, which is not applicable in this case. Therefore, the force balance of particles in this electric field is mainly satisfied among the drag, electric, and Brownian forces. The charged particle trajectory can be described with the following Newton differential equation:

$$m_p\frac{d\vec{u_p}}{dt} = \vec{F}_D + \vec{F}_E + \vec{F}_B \tag{12}$$

The drag force ($\vec{F}_D$) is expressed as:

$$\vec{F}_D = \frac{1}{8}\pi C_d\rho_{gas}d_p{}^2|\vec{u}-\vec{u_p}|(\vec{u}-\vec{u_p}) \tag{13}$$

$$C_d = max\left[\frac{24}{C_cRe_p}\left(1+0.15Re_p^{0.687}\right), 0.44\right] \tag{14}$$

$$C_c = 1+\frac{2\lambda}{dp}\left[1.257+0.4exp\left(-\frac{1.1dp}{2\lambda}\right)\right] \tag{15}$$

The electric force ($\vec{F}_E$) is defined as:

$$\vec{F}_E = q_p\vec{E} \tag{16}$$

The Brownian force ($\vec{F}_B$) is expressed as:

$$\vec{F}_B = \frac{\zeta}{m_p}\sqrt{\frac{1}{D}\frac{2k_B^2T^2}{\Delta t}} \tag{17}$$

$$D = \frac{k_BTC_c}{3\pi\mu d_p} \tag{18}$$

where m_p represents the particle mass, u_p represents the particle velocity, C_d represents the drag coefficient, C_c represents the Cunningham correction factor, Re_p represents the Reynolds number of the particle, λ represents the mean free path of air, ζ is a random number from a zero-mean unit-variance-independent Gaussian probability density function, D represents the Brownian diffusion coefficient, and Δt denotes the time step.

3. Results and discussion

3.1. Generation of ionic wind in the electric field

A schematic of the ESP model applied in this study is shown in Fig. 1a (i). The investigated model consists of two parallel collection plates and three groups of needle-type discharge electrodes. The collection plates are electrically grounded. Meanwhile, the discharge electrode is evenly arranged in the channel, and the negative voltage is selected as 40, 50, or 60 kV. The discharge channel is 720 mm long, 720 mm wide, and 400 mm high. The distance between the needle tip and the collection plate is 160 mm. The dimensions of the needle body and needle tip are displayed in Figs. 1a(ii) and 1a(iii), respectively. The detailed parameters of gas flow, injection particles, and boundary conditions are listed in the Supplementary Materials (Tables S1 and S2).

As a high voltage is applied to the discharge electrode, an electric field is established in the space. Once the applied voltage rises above a critical value, which is called the corona onset voltage, the air surrounding the discharge electrode is ionized, and the ionization region subsequently forms. The produced electrons are accelerated by the
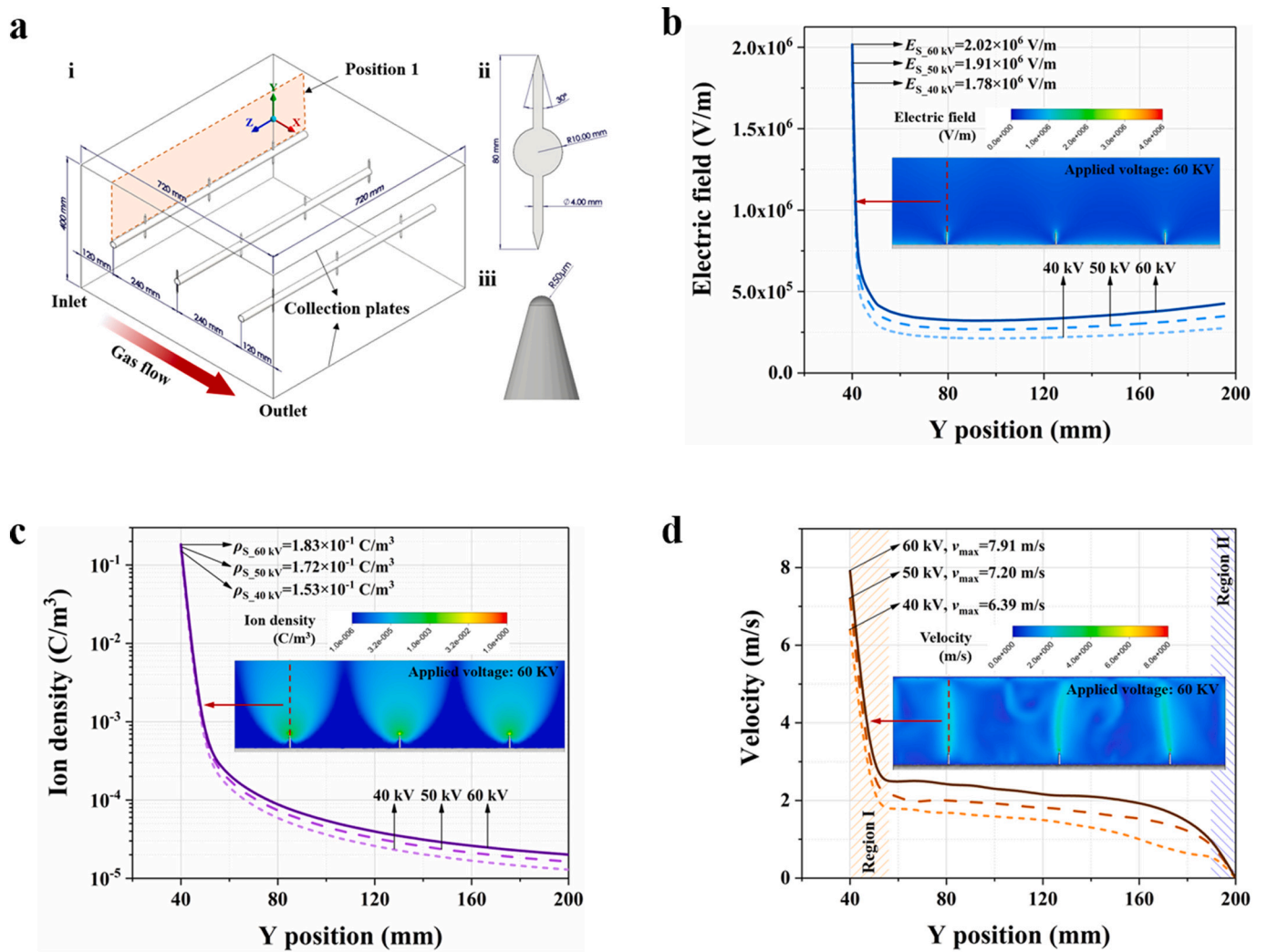
Fig. 1. Generation of ionic wind in the electric field.**a**, Schematic of the typical ESP and dimensions. The emitter is capped with a hemispherical tip of 50 μm in radius. The line distributions of the **b** electric field and **c** ion density are presented under different applied voltages. Both the electric field strength and ion density reach their maximum around the tip of needles, and **d** ionic wind is simultaneously generated in the ionization region. The ionic wind velocity is sharply decreased in regions I and II. The 2D distributions of the electric field, ion density, and flow field at position 1 are shown in the inset of **b**, **c**, and **d**, respectively. A typical applied voltage of 60 kV is selected as an example.

electric field and gain sufficient energy to release more electrons and ions when they collide with other air atoms of the medium. A chain reaction occurs, which is called the electron avalanche. Meanwhile, the electric field pulls electrons and ions in opposite directions to prevent recombination. Beyond a certain distance from the discharge electrode (drift region), sufficient energy can no longer be provided by the electric field to sustain the kinetic energy of electrons for gas ionization. In this region, electrons and ions migrate freely toward the grounded plate, and some are captured by colliding with suspended particles. The distributions of the electric field and ion density field are critical to describing the discharge space, and are depicted in Fig. 1b and c, respectively. The increase in the applied voltage also leads to elevated electric field strength and ion density. The strength of the electric field reaches the maximum around the needles, and rises from 1.78×10^6 V/m to 2.02×10^6 V/m when the applied voltage is raised from 40 kV to 60 kV. The electric field strength dramatically decreases by more than five times compared with the maximum at only 20 mm from the emitter, and then rises slowly along the direction from the needle toward the grounded plate (Y > 80 mm). The inset selects the 2D distribution of 60 kV as an example. As seen in the figure, a low-strength electric field region exists between the needles because of the repulsion effect of the adjacent discharge. Compared with the electric field distribution, the ion density

varies more considerably in different positions. For example, the ion density continuously decreases from 1.83×10^{-1} C/m³ at the needle to 2.01×10^{-5} C/m³ at Y = 200 mm when the applied voltage is 60 kV. Meanwhile, the ion density appears to be discrete with a regular pattern corresponding to the needles, and ion charges may not exist in some regions (e.g., near the cylinder surface or between the needles). For fine particle removal, especially submicron particles, diffusion charging is one of the efficiency-determining steps, which is closely related to the ion density. Therefore, how to improve the uniformity of the ion density distribution by optimizing the electrode geometry or configuration may be an interesting topic to enhance particle charging and precipitation.

The line distribution of the ion wind velocity along the direction from the needle to the collection plate is shown in Fig. 1d, with an inlet velocity of 0.1 m/s. The maximum ion wind velocity appears around the needles because of ionization, and the ionic wind velocity can reach 7.91, 7.20, and 6.39 m/s when negative voltages of 60, 50, and 40 kV are applied to the emitter, respectively. The ionic wind rapidly weakens to approximately 2 m/s due to turbulent dissipation with increasing distance from the needles, as shown in region I. Although the velocity of ionic wind is reduced, it is still faster than other regions, and disturbs the space flow field in a meaningful way, as depicted in the inset of Fig. 1d. A detailed investigation of the role of ionic wind in the space flow field is

discussed in Section 3.2. Meanwhile, the ionic wind is sharply decreased again in the near-plate region because of the boundary layer effect, as shown in region II. The ionic wind will also affect the ion convection; the relationship between the electrostatic field and flow field is a two-way streak.

3.2. Effect of ionic wind on the space flow field

To further investigate the role of ionic wind in the charged flow field, we describe the spatial distribution of the flow field with different presentations. An applied voltage of 60 kV is used as the basic condition to clearly express the effect of ionic wind on the space flow field. The volume renderings of the flow field under different inlet velocities are presented in Fig. 2a. The ionic wind velocity around the needle tip is
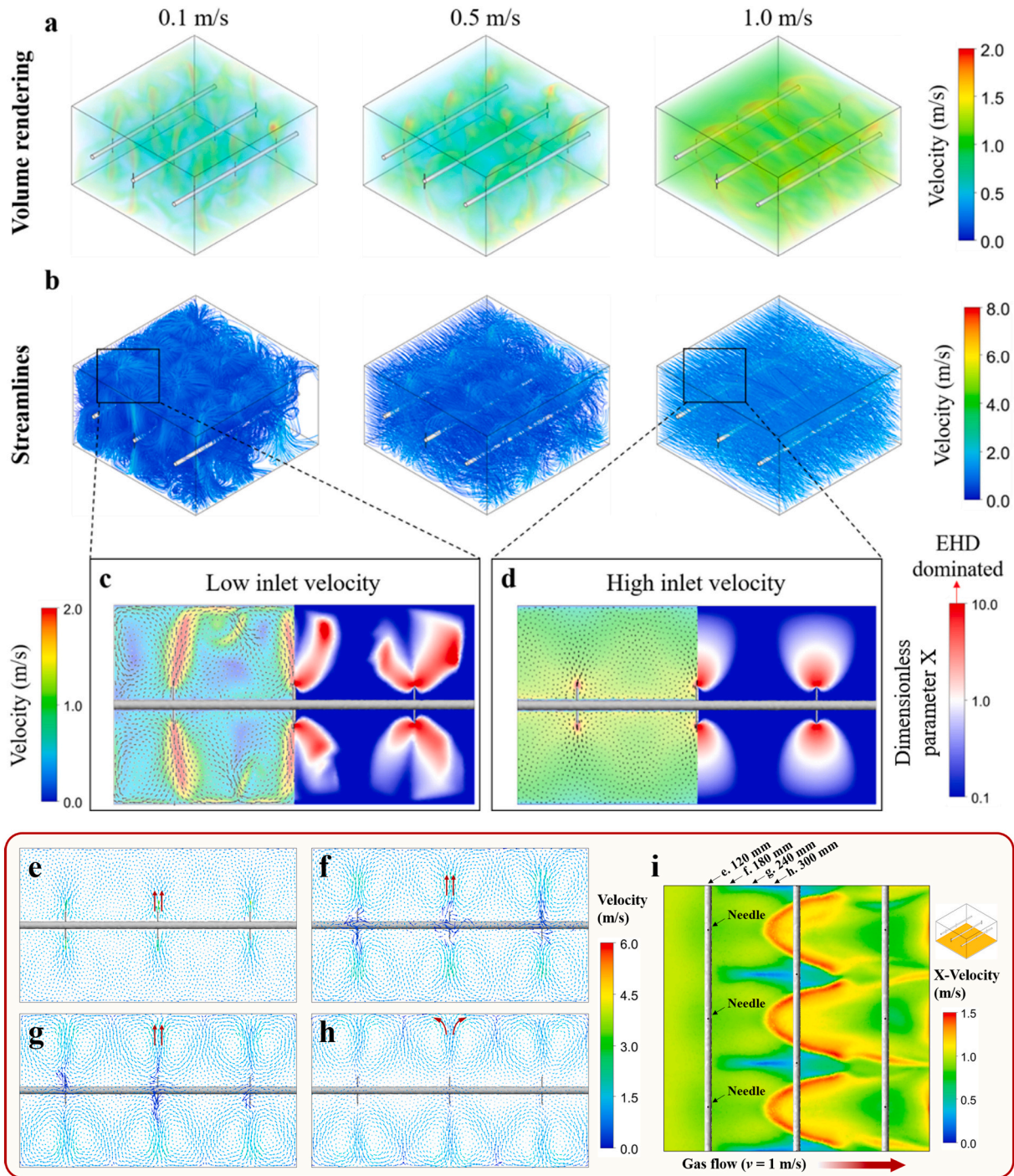

Fig. 2. Disturbance of ionic wind on the space flow field. a volume rendering and **b** streamlines are presented to describe the space flow field disturbed by the ionic wind, and the inlet velocities are set as 0.1, 0.5, or 1.0 m/s. The flow fields in the plane X = 120 mm at **c** low inlet velocity and **d** high inlet velocity are displayed with different characteristics. The left and right graphs show the distributions of the velocity vector and dimensionless parameter X, respectively. The red zone (X > 1) indicates the regions of EHD-dominated flow. Planar gas flow distribution in the planes of **e** X = 120 mm, **f** X = 180 mm, **g** X = 240 mm, and **h** X = 300 mm. The color of the arrows represents the magnitude of the gas flow velocity. The red arrows in these figures represent the direction and the trajectory of high-speed ionic wind. **i**, Contours of gas velocity in the X direction within the near-plate region. The applied voltage is selected as 60 kV for all images.

higher than that in other regions, and the maximum velocity can reach 7.91, 8.05, and 8.54 m/s at inlet velocities of 0.1, 0.5, and 1.0 m/s, respectively. Meanwhile, high-speed regions are formed on both sides of the needles because of the vertical relationship between the generated ionic wind and inlet gas flow. These high-speed regions also shift inward with increasing inlet velocity, and the ends gradually fork to resemble a 'crab claw' shape when the inlet velocity is 1 m/s. This result indicates that the space flow field is significantly disturbed by the high-speed ionic wind (Movies S1 and S2), and the pattern of the space flow field is simultaneously dependent on the applied voltage and initial velocity. To further investigate the disturbance effect of ionic wind on the space flow field, the streamlines under different inlet velocities are visualized in Fig. 2b. At a low inlet velocity (0.1 m/s), the high-speed ionic wind pushes the gas flow moving from near the needle to the grounded plate, creating a shape similar to 'a flower in full bloom' (Movie S3), which is consistent with the EHD structures measured by PIV [26]. This flow field may be conducive to particle transport near the needles. However, the migration of particles also becomes unpredictable as they pass through this ionized flow field. As the inlet velocity increases to 1 m/s, the ionic wind primarily disturbs the downstream flow field near the needles, while the streamlines of the 1 m/s inlet velocity are relatively smooth compared with those of 0.1 m/s.

The above result indicates that the ionic wind drives local flow accelerations. To rationalize these observations, the EHD equation is presented with a dimensionless form to provide further insight into the development of ionic wind in the space electric field [39,40].

$$\text{St}\frac{\partial \vec{u}^*}{\partial t^*}+\left(\vec{u}^*\cdot\nabla^*\right)\vec{u}^* = -\nabla^*P^*+\frac{1}{\text{Fr}^2}\vec{g}^*+\frac{1}{Re}\nabla^{*2}\vec{u}^*-\left[\frac{\rho_{ion}\varphi}{\rho_{gas}\overline{u}^2}\right]\rho_{ion}^*\nabla^*\varphi^*$$

(19)

where St represents the Strouhal number, Fr represents the Froude number, and the asterisk superscript denotes dimensionless variables [41]. Among them, $X = (\rho_{ion}\varphi)/(\rho_{gas}\vec{u}^2)$ is the ratio of electric and inertial terms, which is called the electro-inertial number.

The flow field in the plane where the needles are located (X = 120 mm) at low inlet velocity and high inlet velocity are displayed in Fig. 2c and d, respectively. The left graph shows the velocity vector in the selected plane, with the background as the velocity distribution. The right graph displays the distribution of dimensionless parameter X, which is shown using a blue-to-red contour. In the red zone, which is the EHD-dominated region, the electro-inertial number is greater than the unit, which indicates the region where the electric force is more powerful than the inertial force. At low inlet velocity, the vortices that are indirectly induced by the disturbance of high-speed ionic wind are located at nearly the same plane as the emitters. Meanwhile, the EHD-dominated flow is located on two sides of needles where both the electric field strength and the ion density are high. Notably, although the main flow region of ionic wind also retains the high intensity of electric field strength and ion density, the inertial flow component is higher because of high velocity, which explains why the electro-inertial number is <1 for this region. At high inlet velocity, the ionic wind moves downstream with the main flow, and the velocity distribution is likely to be uniform. The EHD-dominated region is located around the needles in a regular pattern, and the electro-inertial number decreases with the distance from the emitter.

As mentioned above, the downstream flow field will be disturbed by the ionic wind at high inlet velocity. Moreover, the inlet velocity at 1 m/s is the typical condition in the practical application of particle precipitation. Therefore, the planar gas flow distributions perpendicular to the discharge channel in planes e-h with an applied voltage of 60 kV and an inlet velocity of 1 m/s are investigated, as shown in Figs. 2e-2h, respectively. These planes are uniformly spaced from X = 120 mm (the middle of the first discharge electrode) to X = 300 mm with a constant value of 60 mm. In plane e, the gas velocity around the needles is higher than that of other positions because of the generation of ionic wind. Due to ionic wind entrainment, a couple of recirculation eddies are simultaneously induced in the neighboring region around the needles. After the gas flow has passed through the discharge electrode, spherical flows are emitted from needle tips, and the evolution of this EHD flow resembles that of mushroom clouds moving toward the grounded plates, as shown in Fig. 2f and g. The gas flow distribution in plan d indicates that the main flow of high-speed ionic wind is divided into two attenuated gas flows after hitting the plates, and then induced back to the middle and back ends of the discharge channel (see Fig. 2h). Meanwhile, since the movement of the gas flow is blocked by the generated ionic wind, a low-speed zone (with a velocity close to 0 m/s) is detected at the rear end of the needles. The interference then gradually decreases as the plane moves from f to h.

The space flow field is disturbed by the high-speed ionic wind, which also causes the inhomogeneous gas flow distribution on the grounded plates. The gas velocity distribution in the X direction (corresponding to the inlet velocity direction) within the near-plate region is presented to lay the foundation for the next analysis of particle deposition, as shown in Fig. 2i. The main flow of ionic wind moves with the airflow to the downstream region of the discharge electrode, and collides with the grounded plates to form 'U'-shaped high-speed zones. The maximum X-velocity in this zone can reach 1.47 m/s, which is detrimental to the particle deposition process. This high-speed collision may also adversely affect the stability of the formed dust layer, which may be a potential inducer of dust re-entrainment. Therefore, avoiding scouring on the grounded plate by high-speed ionic wind is also an effective method to further improve the efficiency of ESPs, especially when the inlet PM concentration is high.

3.3. Multiple effects of ionic wind on particle transport

Particle migration and deposition are difficult to demonstrate in detail by tracking the trajectory of a single particle. Therefore, a group of electrically neutral particles are uniformly injected into the electric field to investigate the multiple effects of ionic wind on particle transport. The particle trajectories, color scaled according to particle charge, are presented considering different independent variables (i.e., applied voltage, inlet velocity, and particle size), as shown in Fig. S2. After passing through the first discharge electrode, the particles, especially those close to the needles, are all fleetly charged and move toward the grounded plates with the accelerative effects of ionic wind propulsion and electric force.

To further investigate this topic, the particle transport around the needles and the particle deposition are discussed in detail (Fig. 3a). The data in Fig. 3b and Movie S4 indicate that the particle velocity in the Y direction (the velocity component toward the grounded plates) rises rapidly with the acceleration of ionic wind propulsion and electric force, especially when passing through the needles. Selecting a 1 μm particle as an example, the maximum particle velocity in the Y direction can reach 197.50 cm/s, which is significantly higher than its typical migration velocity. Meanwhile, the particle deflection — introduced by drag and electric forces — is gradually increased as the particle size increases from 1 μm to 30 μm. The effect of ionic wind propulsion and electric force on particle migration will eventually be reflected in the distribution of particle deposition. As shown in Fig. 3c, for nano-scale particles (100 nm, such as sulfuric acid aerosol or virus), the distribution of deposited particles is relatively uniform, and the particle deposition is slightly enhanced downstream of the electrode. Figs. 3d-3f indicate that the micron-scale particle deposition is greatly affected by the ionic wind, and exhibits more obvious changes with particle size. The number concentration of deposited particles is significantly increased upstream, owing to the vortex generated by the ionic wind disturbance dragging the particles upstream, and the maximum number concentration can reach 59 mm^{-2} when 2×10^7 particles are injected into the electric field. Furthermore, the particle deposition is enhanced again around the third
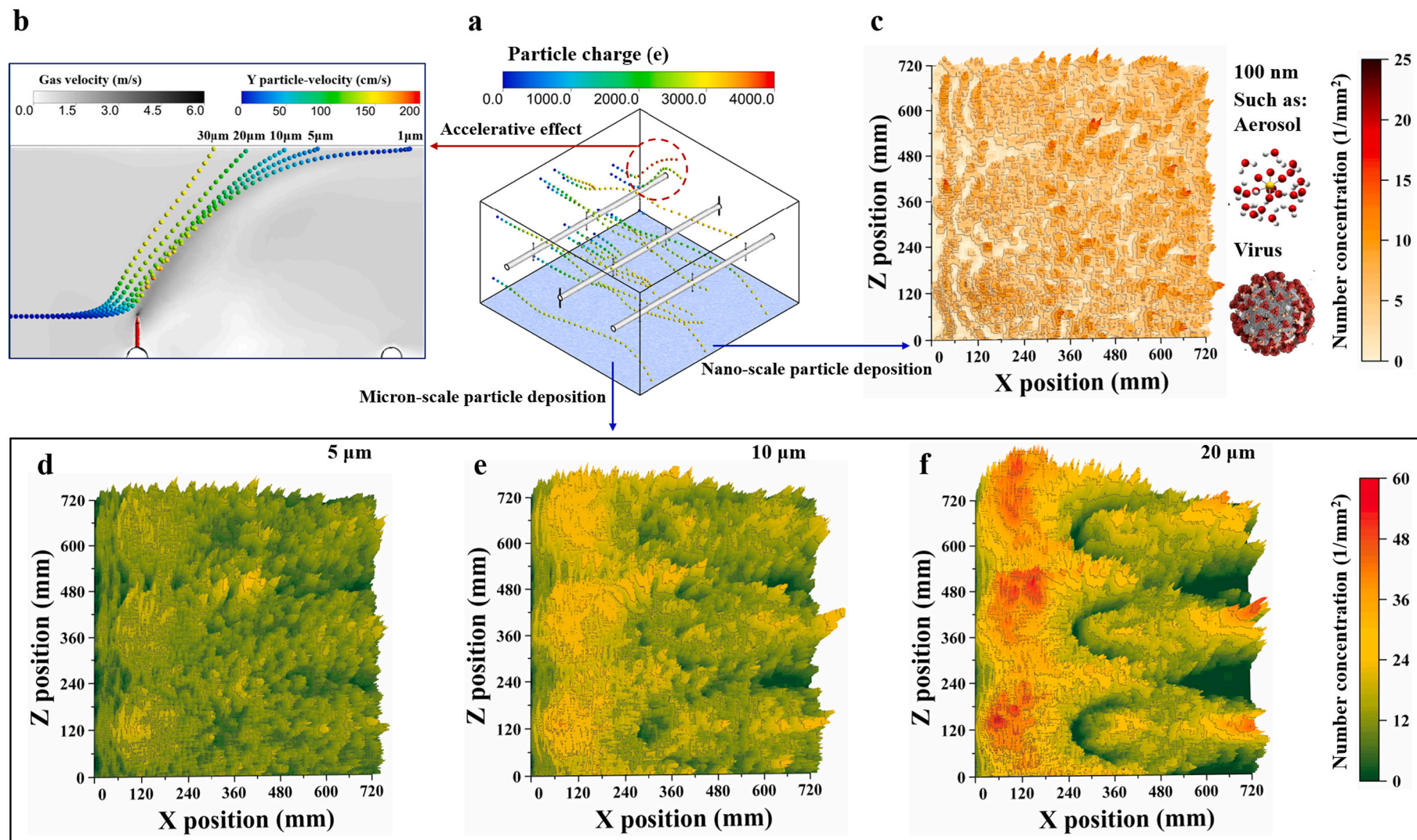
Fig. 3. Transport of charged particles by ionic wind propulsion in the electric field.a, Particle trajectories in the electric field and color scaled according to particle charge. **b,** The particle trajectories with color scaled according to particle velocity in the Y direction. These 1–30 μm particles are injected into the electric field at the same location (X = 0, Y = 40 mm, Z = 360 mm) in turn. The background is the planar gas-velocity distribution, which indicates the accelerative effect of high-speed ionic wind on charged particle transport in the electric field. At the same time, the distribution of deposited particles with diameters of **c** 100 nm, **d** 5 μm, **e** 10 μm, and **f** 20 μm on the grounded plates are presented. The number of injected particles in **c, d, e,** and **f** are all 2×10^7. The applied voltage is selected as 60 kV and the inlet velocity is set as 1.0 m/s for all images.

discharge electrode. Simultaneously, the particle deposition is obviously weakened in the high-speed region of the near-plate region, causing the 'unoccupied areas'. This phenomenon can be attributed to the fact that the accelerated gas velocity reduces the particle deposition time, which further deteriorates with particle size. Particle deposition on the grounded plates increases with the applied voltage. Meanwhile, the unoccupied areas, although they still persist, will be further reduced and moved forward by the enhanced ionic wind propulsion (Fig. S3). Eventually, 'every coin has two sides'.

For nano-scale particles, the distribution of deposited particles is relatively uniform. However, the deposition of micron-scale particles is greatly affected by the ionic wind, and exhibits more obvious changes with particle size. This result gives a fundamental principle for the design and efficiency improvement of gas purification equipment. In indoor air purification, the possible means to inactivate airborne infectious agents have been intensively investigated and have been subject to intense debates [42]. Viruses and bacteria can be charged and partially inactivated after entering the electric field, and are transported to the grounded plates with ionic wind propulsion and electric force [43]. Further scouring of the grounded plates with disinfectants is a possible approach to further improve the bactericidal effect, and it should be strengthened downstream according to the distribution of deposition.

Meanwhile, particle electrostatic precipitation is also extensively used to remove dust in various fields of industrial application, such as coal-fired power plants and metallurgical industries. The mean particle size of these flue gases is approximately 20 μm [44,45]. The increase in upstream particle deposition will induce the spark within the dust layer (back corona), while dust re-entrainment occurs more easily with the accelerative airflow. The careful design of the grounded plate according to the particle deposition performance may be a potential means to further improve particle electrostatic precipitation.

3.4. Countermeasures for optimizing the flow field and particle removal enhancement

As mentioned above, particle migration is enhanced with the acceleration of ionic wind, but also causes the formation of 'U'-shaped high-speed zones within the near-plate region, which will aggravate the occurrence of back corona and dust re-entrainment. Therefore, a novel electrode configuration is proposed to overcome the above disadvantages by optimizing the space flow field and particle precipitation performance.

The design of this ESP is uncomplicated but useful. The addition of perforated plates at a distance of 40 mm from the grounded plate is shown in Fig. S4. The perforated plates are grounded, and the particles
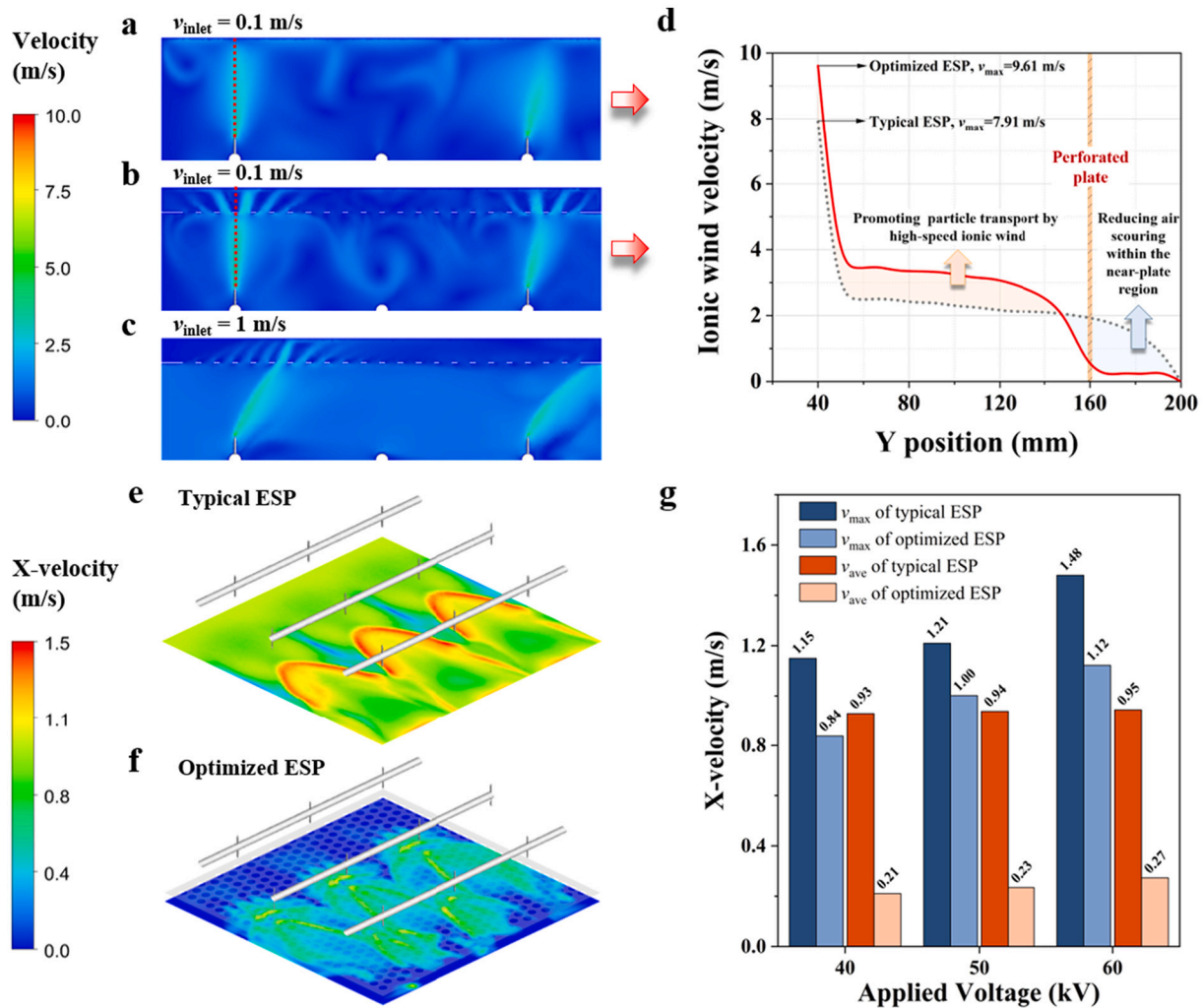

Fig. 4. Effect of the perforated plate on the space flow field performance. a, Flow field distribution of the typical ESP under an inlet velocity of 0.1 m/s. The flow field distributions of the optimized ESP under inlet velocities are **b** 0.1 m/s and **c** 1 m/s. **d,** Line distribution of ionic wind velocity along the needle direction. Comparison of **e** typical ESP and **f** optimized ESP on X-velocity within the near-plate region. **g,** Variation in the X-velocity for typical and optimized ESPs under different applied voltages. The applied voltage is selected as 60 kV for all images unless specified.

colliding with perforated plates are considered to be deposited. The distributions of the electric field, ion density, and current density indicate that the electrostatic characteristics of the region between the grounded and perforated plates are weak, which contributes to avoiding the spark within the dust layer (Figs. S5 and S6). Apart from the optimization of electrostatic characteristics, the improvement of the space flow field by adding perforated plates should not be underestimated. The high-speed ionic wind is diluted when passing through the perforated plate, as shown in Figs. 4a-4c. Meanwhile, the corona discharge performance of ESP is enhanced because of the shorter distance between the electrodes. This is also reflected in the ionic wind velocity. As illustrated in Fig. 4d, the maximum ionic wind velocity is increased from 7.91 m/s to 9.61 m/s compared with the typical ESP. On the one hand, the higher ionic wind velocity, in the region between the discharge electrode and the perforated plate, promotes particle migration toward the grounded plates. On the other hand, the ionic wind velocity is decreased near the perforated plate, which obviously reduces the scouring of ionic wind on grounding plates (Figs. 4e-4f). For instance, the maximum and average velocities in the X direction within the near-plate region are reduced from 1.48 m/s and 0.95 m/s to 1.12 m/s and 0.27 m/s, respectively, under an applied voltage of 60 kV (Fig. 4g). The probability of re-entrainment will be significantly reduced. Meanwhile, the presence of perforated plates increases the turbulence intensity of flue gas, which contributes to the particle deposition process.

Compared with the typical ESP, the deposited particle distribution of the optimized ESP is more uniform, as shown in Fig. 5a. The addition of perforated plates significantly reduces the deposition of particles around the discharge electrode, while compensating for the 'unoccupied areas' of the dust layer. The reduction in dust layer thickness around the discharge electrode can effectively prevent the accumulation of charges (Fig. 5b). Meanwhile, the electric field strength of the region between the perforated and grounded plates is significantly lower than that of a typical ESP, which introduces a reduction in the electric field strength within the dust layer. Therefore, the occurrence of back corona can be efficiently avoided by using this optimized ESP. Moreover, the addition of perforated plates can significantly reduce dust re-entrainment. As shown in Fig. 5c, although the deposited particles are still blown up by the high-speed ionic wind, they will continue to migrate onto perforated or grounded plates under the action of electric force. The perforated plate will also provide a restraint for particles that try to escape from the region between perforated and grounded plates, which is beneficial for the shaking process of ESPs. The improvement of the optimized ESP in particle collection efficiency is illustrated in Fig. 5d. For particles with diameters of 100 nm, 5 μm, 10 μm, and 20 μm, the collection efficiency is enhanced by 57.6%, 41.3%, 30.4%, and 12.1%, respectively.

Ionic wind plays a vital role in charged particle removal during flue gas purification due to flow field disturbance. Thus, rationally using ionic wind should be specifically considered in the future-oriented design of gas purification equipment to realize air quality improvement. This research provides new thinking for the investigation of charged particle behaviors and flue gas purification. The optimized ESP mentioned above is just an example, and the application of ionic wind can also be reflected in other aspects. In our previous research [46,47], some results indicated that electrons can activate particle growth substantially. Therefore, collisional coupling between ionized gases (ionic wind) and particles/droplets also seems to be a possible way to mitigate pollutant emissions. Meanwhile, since the local velocity near the needles is too high to be neglected compared with the ion drift velocity, its effect on the electric field may be an interesting topic for future studies. In addition, ionic wind can modify streamer generation and propagation, which alters the efficient transport of long-lived species (e.g., particles, viruses, ozone, and nitrogen oxides) with lifetimes ranging from milliseconds to minutes due to the enhanced airflow [48]. Further improvements in these two performance limitations of particle directional transportation and overall efficiency could open up new design spaces for ionic wind propulsion and explore its extraordinary application fields.
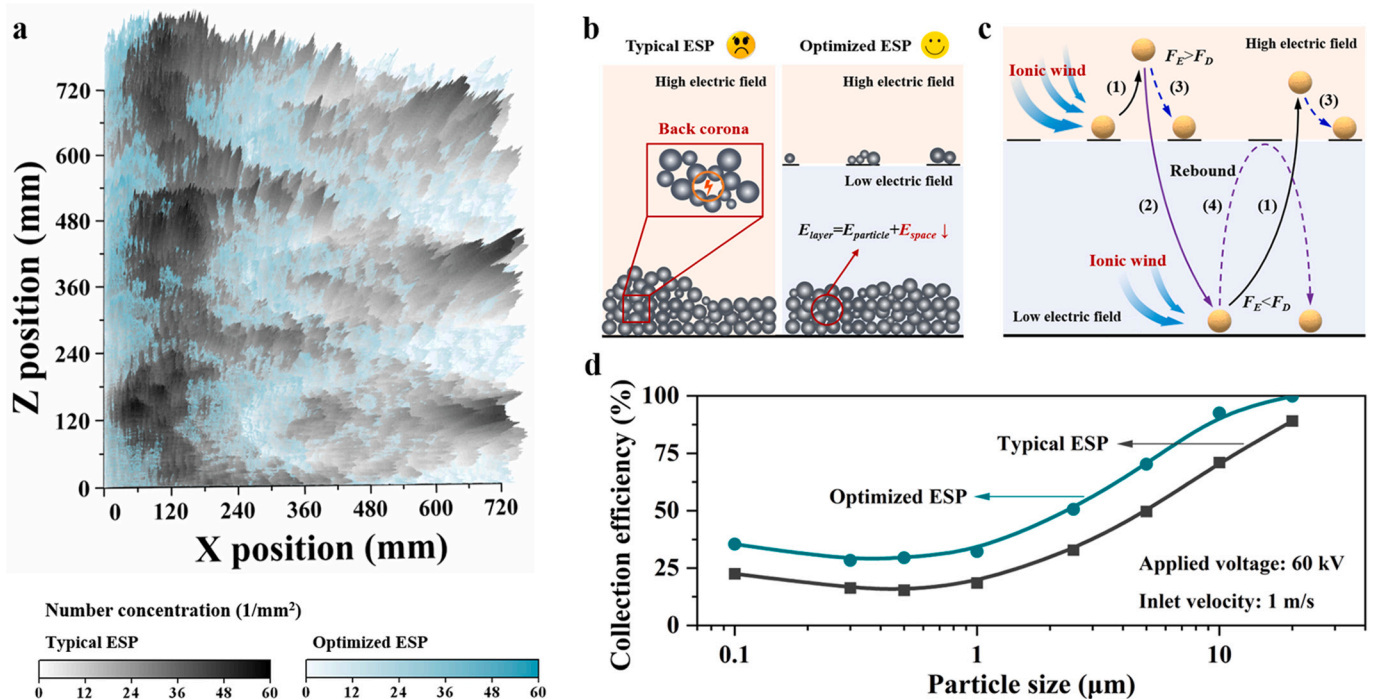

Fig. 5. Enhancing particle removal performance by an optimized ESP. **a**, comparison of typical and optimized ESPs on 20 μm deposited particle distribution, and the number of injected particles is 2×10^7. **b**, Schematic of the differences in particle deposition and back corona performance for typical and optimized ESPs. **c**, Schematic of the role of the perforated plate in particle deposition and re-entrainment. Step (1) represents particle re-entrainment due to ionic wind blowing. Steps (2) and (3) represent particles redeposit on the grounded and perforated plates when $F_E > F_D$, respectively. Step (4) represents particle re-entrainment due to ionic wind blowing, but bounces back after a collision with the perforated plate. **d**, Improvement of optimized ESP in particle collection efficiency.

4. Conclusion

In summary, a comprehensive model is established to investigate the effect of ionic wind on space flow field disturbance and charged particle migration. Ions are generated at the tips of a conductor, and the momentum of these accelerated ions is coupled with that of the bulk fluid, thus forming high-speed ionic wind. The ionic wind velocity can reach 7.91 m/s when a negative voltage of 60 kV is applied to the emitter, which is significantly higher than the inlet velocity. The high-speed ionic wind strongly disturbs the space flow field, and causes the formation of 'U'-shaped high-speed zones within the near-plate region. The maximum X-velocity in this zone can reach 1.47 m/s, which is detrimental to the particle deposition process. After the dusty flue gas enters the electrostatic field, the particle velocity rapidly increases with the acceleration of ionic wind propulsion, especially when passing through the needles, which is beneficial to particle removal. Meanwhile, the uneven distribution of deposited particles, resulting from ionic wind propulsion, will further induce the spark within the dust layer (back corona) and re-entrainment. Based on these findings, a novel electrostatic precipitator is proposed to overcome the adverse effects of ionic wind, and the collection efficiency and dust layer shape are both significantly improved. The particle collection efficiency of 100 nm, 5 μm, 10 μm, and 20 μm could be enhanced by 57.6%, 41.3%, 30.4%, and 12.1%, respectively. This work provides the cornerstone for the future-oriented design of flue gas purification by rationally using ionic wind to achieve a lower pollutant emission level.

Declaration of Competing Interest

The authors have no conflicts of interest to declare.

Data availability

Data will be made available on request.

Acknowledgments

Appendix A. Supplementary data

Supplementary data to this article can be found online at https://doi.org/10.1016/j.powtec.2022.117804.

References

[1] O. Hoegh-Guldberg, D. Jacob, M. Taylor, et al., The human imperative of stabilizing global climate change at 1.5°C, Science 365 (6459) (2019) eaaw6974.

[2] I. Manisalidis, E. Stavropoulou, A. Stavropoulos, et al., Environmental and health impacts of air pollution: a review, Front. Public Health 8 (2020).

[3] J. Wu, F. Tou, Y. Yang, et al., Metal-containing nanoparticles in low-rank coal-derived fly ash from China: characterization and implications toward human lung toxicity, Environ. Sci. Technol. 55 (10) (2021) 6644–6654.

[4] Y. Zheng, Q. Chen, X. Cheng, et al., Precursors and pathways leading to enhanced secondary organic aerosol formation during severe haze episodes, Environ. Sci. Technol. 55 (23) (2021) 15680–15693.

[5] X. Zeng, S. Kong, Q. Zhang, et al., Source profiles and emission factors of organic and inorganic species in fine particles emitted from the ultra-low emission power plant and typical industries, Sci. Total Environ. 789 (2021), 147966.

[6] A. Jaworek, A.T. Sobczyk, A. Marchewicz, et al., Particulate matter emission control from small residential boilers after biomass combustion. A review, Renew. Sust. Energ. Rev. 137 (2021) 110446.

[7] C. Zheng, Y. Wang, Y. Liu, et al., Formation, transformation, measurement, and control of SO3 in coal-fired power plants, Fuel 241 (2019) 327–346.

[8] B. Wu, H. Tian, Y. Hao, et al., Effects of wet flue gas desulfurization and wet electrostatic precipitators on emission characteristics of particulate matter and its ionic compositions from four 300 MW level ultralow coal-fired power plants, Environ. Sci. Technol. 52 (23) (2018) 14015–14026.

[9] Y. Zeng, R. Xie, J. Cao, et al., Simultaneous removal of multiple indoor-air pollutants using a combined process of electrostatic precipitation and catalytic decomposition, Chem. Eng. J. 388 (2020), 124219.

[10] L. Chen, E. Gonze, M. Ondarts, et al., Electrostatic precipitator for fine and ultrafine particle removal from indoor air environments, Sep. Purif. Technol. 247 (2020), 116964.

[11] B. Farr, X. Wang, J. Goree, et al., Improvement of the electron beam (e-beam) lunar dust mitigation technology with varying the beam incident angle, Acta Astronaut 188 (2021) 362–366.

[12] R.S. Islamov, Analysis of the dynamics of dust reentrainment with simultaneous electrostatic deposition and without any deposition after a jump of airflow velocity, J. Aerosol Sci. 144 (2020), 105533.

[13] A. Jaworek, A. Marchewicz, A.T. Sobczyk, et al., Two-stage electrostatic precipitators for the reduction of PM2.5 particle emission, Prog. Energy Combust. Sci. 67 (2018) 206–233.

[14] Y. Zhu, M. Gao, M. Chen, et al., Numerical simulation of capture process of fine particles in electrostatic precipitators under consideration of electrohydrodynamics flow, Powder Technol. 354 (2019) 653–675.

[15] H. Pu, J. Guo, H. Qu, et al., Fine particle transport and deposition characteristics in a spike-plate multi-electrode electrostatic precipitator, Powder Technol. 402 (2022), 117339.

[16] J. Zhang, L. Kong, J. Qu, et al., Numerical and experimental investigation on configuration optimization of the large-size ionic wind pump, Energy 171 (2019) 624–630.

[17] S. Park, U. Cvelbar, W. Choe, et al., The creation of electric wind due to the electrohydrodynamic force, Nat. Commun. 9 (1) (2018) 371.

[18] J. Wang, T. Zhu, Y.-X. Cai, et al., Review on the recent development of corona wind and its application in heat transfer enhancement, Int. J. Heat Mass Transf. 152 (2020) 119545.

[19] J. Gu, G. Zhang, Q. Wang, et al., Experimental study on particles directed transport by an alternating travelling-wave electrostatic field, Powder Technol. 117107 (2022).

[20] E. Moreau, P. Audier, N. Benard, Ionic wind produced by positive and negative corona discharges in air, J. Electrost. 93 (2018) 85–96.

[21] Y. Wang, H. Zhang, W. Gao, et al., Improving the removal of particles via electrostatic precipitator by optimizing the corona wire arrangement, Powder Technol. 388 (2021) 201–211.

[22] Y. Tong, L. Liu, L. Zhang, et al., Separation of fine particulates using a honeycomb tube electrostatic precipitator equipped with arista electrodes, Sep. Purif. Technol. 236 (2020), 116299.

[23] C. Zheng, X. Zhang, Z. Yang, et al., Numerical simulation of corona discharge and particle transport behavior with the particle space charge effect, J. Aerosol Sci. 118 (2018) 22–33.

[24] A. Krupa, J. Podliński, J. Mizeraczyk, et al., Velocity field of EHD flow during back corona discharge in electrostatic precipitator, Powder Technol. 344 (2019) 475–486.

[25] J. Podlinski, A. Berendt, J. Mizeraczyk, Electrohydrodynamic secondary flow and particle collection efficiency in spike-plate multi-electrode electrostatic precipitator, IEEE Transact. Dielectr. Electr. Insulat. 20 (5) (2013) 1481–1488.

[26] J. Mizeraczyk, A. Berendt, J. Podlinski, Temporal and spatial evolution of EHD particle flow onset in air in a needle-to-plate negative DC corona discharge, J. Phys. D. Appl. Phys. 49 (20) (2016), 205203.

[27] S. Li, M. Li, J. Ma, et al., Characterization of electrohydrodynamic flow in a plate-plate electrostatic precipitator with a wire-cylinder pre-charger by data-driven vortex and residence time analysis, Powder Technol. 397 (2022), 117015.

[28] K. Adamiak, Numerical models in simulating wire-plate electrostatic precipitators: a review, J. Electrost. 71 (4) (2013) 673–680.

[29] D. Yang, B. Guo, X. Ye, et al., Numerical simulation of electrostatic precipitator considering the dust particle space charge, Powder Technol. 354 (2019) 552–560.

[30] K. Luo, Y. Li, C.H. Zheng, et al., Numerical simulation of temperature effect on particles behavior via electrostatic precipitators, Appl. Therm. Eng. 88 (2015) 127–139.

[31] W. Zhou, R. Jiang, Y. Sun, et al., Study on multi-physical field characteristics of electrostatic precipitator with different collecting electrodes, Powder Technol. 381 (2021) 412–420.

[32] G.-H. Lee, S.-Y. Hwang, T.-W. Cheon, et al., Optimization of pipe-and-spike discharge electrode shape for improving electrostatic precipitator collection efficiency, Powder Technol. 379 (2021) 241–250.

[33] Y. Wang, W. Gao, H. Zhang, et al., Insights into the role of ionic wind in honeycomb electrostatic precipitators, J. Aerosol Sci. 133 (2019) 83–95.

[34] K.R. Parker, Applied Electrostatic Precipitation, Springer Science & Business Media, 2012.

[35] C.H. Zheng, Q.Y. Chang, Q.Y. Lu, et al., Developments in unipolar charging of airborne particles: theories, simulations and measurements, Aerosol Air Qual. Res. 16 (12) (2016) 3037–3054.

[36] Z. Long, Q. Yao, Evaluation of various particle charging models for simulating particle dynamics in electrostatic precipitators, J. Aerosol Sci. 41 (7) (2010) 702–718.

[37] P.A. Lawless, Particle charging bounds, symmetry relations, and an analytic charging rate model for the continuum regime, J. Aerosol Sci. 27 (2) (1996) 191–215.

[38] S.C. Garrick, M. Bühlmann, Modeling of Gas-to-Particle Mass Transfer in Turbulent Flows, Springer, 2018.

[39] Y.F. Guan, R.S. Vaddi, A. Aliseda, et al., Experimental and numerical investigation of electrohydrodynamic flow in a point-to-ring corona discharge, Physical Review Fluids 3 (4) (2018), 043701.

[40] J. Shrimpton, Charge Injection Systems: Physical Principles, Experimental and Theoretical Work, Springer Science & Business Media, 2009.

[41] B.R. Munson, T.H. Okiishi, W.W. Huebsch, et al., Fluid Mechanics, Wiley Singapore, 2013.

[42] X.R. Hu, M.F. Han, C. Wang, et al., A short review of bioaerosol emissions from gas bioreactors: health threats, influencing factors and control technologies, Chemosphere 253 (2020), 126737.

[43] S.S. Narayanan, X. Wang, J. Paul, et al., Disinfection and electrostatic recovery of N95 respirators by Corona discharge for safe reuse, Environ. Sci. Technol. 55 (22) (2021) 15351–15360.

[44] B. Wu, X. Bai, W. Liu, et al., Variation characteristics of final size-segregated PM emissions from ultralow emission coal-fired power plants in China, Environ. Pollut. 259 (2020), 113886.

[45] B. Wu, H. Tian, Y. Hao, et al., Refined assessment of size-fractioned particulate matter (PM2.5/PM10/PMtotal) emissions from coal-fired power plants in China, Sci. Total Environ. 706 (2020) 135735.

[46] Z. Yang, C. Zheng, Q. Li, et al., Fast evolution of sulfuric acid aerosol activated by external fields for enhanced emission control, Environ. Sci. Technol. 54 (5) (2020) 3022–3031.

[47] C. Zheng, H. Zheng, J. Shen, et al., Evolution of condensable fine particle size distribution in simulated flue gas by external regulation for growth enhancement, Environ. Sci. Technol. 54 (7) (2020) 3840–3848.

[48] N. Misra, A. Martynenko, F. Chemat, et al., Thermodynamics, transport phenomena, and electrochemistry of external field-assisted nonthermal food technologies, Crit. Rev. Food Sci. Nutr. 58 (11) (2018) 1832–1863.